Multiscale investigation of the microstructural mechanisms driving ratchet growth in PBX 9502

Yeager, John David
Montanari, Danielle Elizabeth
Woznick, Caitlin Savanna
Knepper, Robert
Bennett, Kane

To be published in: Journal of Energetic Materials

DOI to publisher's version: 10.1080/07370652.2022.2032485

Multiscale investigation of the microstructural mechanisms driving ratchet growth in PBX 9502

J. D. Yeager,[1*] D. Montanari,[1] C. Woznick,[1] R. Knepper,[2] K. C. Bennett.[3]

1. High Explosives Science and Technology, Los Alamos National Laboratory, Los Alamos, NM 87545

2. Explosive Technologies Group, Sandia National Laboratories, Albuquerque, NM 87185

3. Geophysics, Los Alamos National Laboratory, Los Alamos, NM 87545

* email: jyeager@lanl.gov; ph: 505-665-0879

This accepted manuscript has been published in the Journal of Energetic Materials, January 2022, and can be found online at https://doi.org/10.1080/07370652.2022.2032485

Abstract

The high explosive PBX 9502 undergoes irreversible expansion during thermal cycling ("ratchet growth"). Recent innovations in thermomechanical modeling via homogenization strategies are beginning to incorporate mesoscale information such as grain size, total porosity, and spatial distribution of voids and cracks. To generate a complete experimental data set to challenge and inform these models, PBX 9502 pellets were thermally cycled, cross-sectioned using ion polishing, and imaged in high resolution with scanning electron microscopy. Ratchet growth was found to drive expansion through microcracking. Microcracks were affected by agglomeration of crystals within the PBX. Virgin material showed greater ratchet growth than recycled material.

1. Introduction

Triaminotrinitrobenzene (TATB) is a high explosive that is remarkably insensitive to mechanical insult. TATB, and its associated plastic-bonded explosive (PBX) formulations, undergo irreversible thermal expansion ("ratchet growth") upon thermal cycling [1-4]. Explorations of ratchet growth have been numerous, and at least several researchers have posited driving mechanisms to explain this behavior[5-8]. These range from atomic to microstructural in nature. TATB crystals are roughly graphitic in morphology, with a triclinic crystal structure where the basal planes (*a*-*b*) are weakly bonded to each other in the *c*-direction [9]. All of these factors combine to result in a material that is highly thermomechanically anisotropic at the atomic scale as well as the grain scale. The irregular shape of the crystals may also play a role in the development of crystal orientation anisotropy, or texture, in consolidated parts [10, 11]. Numerous studies of TATB and PBX 9502 (95 wt% TATB, 5 wt% Kel-F 800 polymer) have shown evidence for asymmetric thermal and mechanical properties as a result of anisotropic crystal orientation [11, 12]. The exact nature of the relationships between crystal anisotropy, texture, and ratchet growth are currently not well-defined in the literature, but the interactions

and interfaces between bonded particles must play some role because TATB single crystals and loose powder do not exhibit ratchet growth [7, 10].

Part of the difficulty in discovering the underlying mechanisms of ratchet growth is the lack of ability to characterize certain properties of TATB. TATB itself is highly insoluble and so single crystals cannot be grown to a large enough size to be measured by all desired techniques. For example, the full elastic tensor of TATB has never been measured and is only available through calculations [13, 14]. TATB, like most high explosives, is relatively fragile, and it tends to clump in powder form and when formulated with a polymer binder. While the polymer binder does give mechanical stability, enabling manufacturing and machining to prepare convenient specimens, typical microstructural characterization techniques are made difficult by the poor optical and electronic contrast between the crystals and the binder [15]. Nonetheless, optical microscopy can be useful when done carefully, showing for example that "virgin" PBX 9502 has larger grain sizes than "recycled" PBX 9502, which incorporated reprocessed TATB from other PBX batches into the formulation [16]. In either case, the TATB crystals are generally sub-50 μm and are often sub-10 μm [17-19], suggesting that scanning electron microscopy (SEM) might be a more suitable choice for imaging the microstructure. Indeed, several studies have used SEM imaging on PBX 9502 to attempt to study grain size, fracture surfaces, and even the effects of ratchet growth [5, 6]. However, sample preparation is always an issue, as polishing the PBX pellets can be difficult. Non-destructive imaging techniques, primarily x-ray computed tomography, have been used with some success to examine voids, cracks, and grain agglomeration, but do not have the spatial resolution of SEM [15, 20].

Recent advancements in microscale characterization and analysis of explosives have the potential to greatly improve our understanding of the effects of ratchet growth on explosive performance, as recent PBX modeling efforts have begun to incorporate discrete mesoscale data to improve prediction of explosive properties. These range from void-based reactive burn models for detonation physics [21-23] to self-consistent homogenization models for thermomechanical behavior [24, 25]. These models have reached a level of sophistication where high-fidelity descriptions of void morphology (e.g., not just overall porosity or average void size) are highly relevant. Ultrasmall angle neutron scattering (USANS), for example, can easily measure a void size distribution by assuming spherical voids [26], but some results in TATB have indicated that the voids are more likely elongated and even networked [27]. Traditionally, these elongated and interconnected voids would be termed "cracks" and consequently require different treatment in models than isolated voids [24, 28, 29].

Identification and characterization of voids and cracks are therefore important to both the PBX mechanics and PBX detonation communities. Here, in an effort to distinguish between the formation of isolated voids and cracks in ratchet growth of PBX 9502, we present an SEM-based study on pristine and ratchet-grown material. Samples are prepared from typical compaction processes and then thermally cycled while measuring axial displacement and strain. We avoid traditionally difficult sample preparation by using a broad beam ion polisher to create a smooth cross-section immediately before imaging. We study both virgin and recycled lots of PBX 9502, which to our knowledge is the first direct comparison of ratchet growth behavior in the two

materials. Image analysis was used to determine overall void content as well as void morphology as a function of ratchet growth. Apparent microcracking associated with ratchet growth was also analyzed, as well as its contribution to void measurements. Observations of microcrack morphology associated predominantly with apparent particle interfaces are examined. Discussion of how these data can be implemented in models moving forward will be presented. We adopt the terminology herein of distinguishing between crystal grains and agglomerates, where we refer to both interchangeably as "particles."

2. Experimental

2.1 Sample Preparation and Thermal Cycling

PBX 9502 virgin and recycled lots were supplied from legacy reserves. Both lots were die pressed into small cylinders approximately 3 mm length by 3 mm diameter. Pressing was performed at 50°C, and the pellets were pressed to average density of 1.889 ± 0.003 g/cm^2.

All thermal cycling tests were performed on a TA Instruments Thermal Mechanical Analyzer (TMA) Q400. For all tests, a single cycle consists of a 30 minute hold at 23°C, ramp up to 153°C for a 30 minute hold, ramp down to ambient again for another 30 minute hold, ramp down to -53°C for a 30 minute hold, and finally a ramp up back to ambient for a 30 minute hold. All ramp rates were 1°C/min. Two specimens of each lot were cycled 10 times and one specimen each was cycled once. The 10 cycle tests were used to compare ratchet growth response of the virgin and recycled lots. The once-cycled tests, as well as the first cycle of the 10-cycle tests, were used to compare coefficient of thermal expansion (CTE) response of the two lots. It is important to note that the strain measured on each specimen is in the axial direction of the cylindrical specimens. During pressing of TATB into cylinders, Schwarz et al. found that the TATB platelets tend to align perpendicular to the pressing direction [11]. Therefore, strain is measured along the pressing direction, normal to the platelet surface, which is the direction of the most growth [30]. Volumetric expansion can be estimated from this axial measurement where the diametral expansion is estimated to be 70% of the axial measurement [31].

2.2 SEM Characterization

Six of the pellets (3 virgin, 3 recycled) were shipped to Sandia National Laboratories for cross-sectioning and SEM analysis. Table 1 shows the sample details. Initial attempts were made to prepare sufficient quality sample surfaces using in-situ focused ion beam (FIB) milling. This technique has been used with reasonable success on some other HE samples recently [32, 33]. However, the PBX samples were quite soft and easily damaged by the milling, such that the subtle microstructural features (e.g., voids) were somewhat difficult to quantitatively measure with so many FIB-induced defects and curtaining artifacts. All samples were therefore prepared *ex situ* to the SEM using a broadbeam argon ion mill (Hitachi IM4000 Plus) operating at 6 kV and 70 μA, in a similar way to previously established efforts [34, 35]. A ±40° stage swing was used to improve uniformity of the ion-polished surface and minimize curtaining artifacts. Multiple cuts were performed so that the section analyzed was several hundred microns from the

outer edge of the pellet; however, a center cut was not used, due to the prohibitive time and material costs of milling half of each pellet away. This process resulted in several mm^2 of reasonably clean surface area per pellet. Subsequent SEM imaging was performed using the secondary electron detector and a 1.1 kV accelerating voltage.

Table 1. List of the 6 Samples for SEM Analysis

Sample	Lot	# Thermal Cycles
R-0	Recycled	0 – Pristine
R-1	Recycled	1
R-10	Recycled	10
V-0	Virgin	0 – Pristine
V-1	Virgin	1
V-10	Virgin	10

The cross-section surfaces were not completely centered in the pellet but were far enough from the outer edge as to avoid any potential skin effects. Multiple images were taken of the sectioned surfaces at two different spatial resolutions. Figure 1 shows a schematic of the nominal imaging plan. In reality, some images were taken at slightly different locations to avoid any large artifacts (debris, scratches) induced by the sectioning. Each image location was tracked with x- and y-Cartesian coordinates. Many high-resolution images were taken with a 50 μm field of view (FOV) and a resolution of 12.2 nm/pixel; larger FOV images (400 and 800 μm) were taken at lower resolution (195 nm/pixel). Note that the images are rectangular at a 4(x):3(y) ratio, but for convenience the x-value is used here as the label of the FOV. The goal was to have a small amount of overlap between the large and small FOV images so that correlations could be made between different FOV and with respect to the apparent measured damage. Some of the 50 μm images also contained a small amount of overlap so that they could be virtually stitched together to create a larger representative area for future analysis or simulations. Each pellet had at least 20 images taken with a total imaged area of just over 1 mm^2.

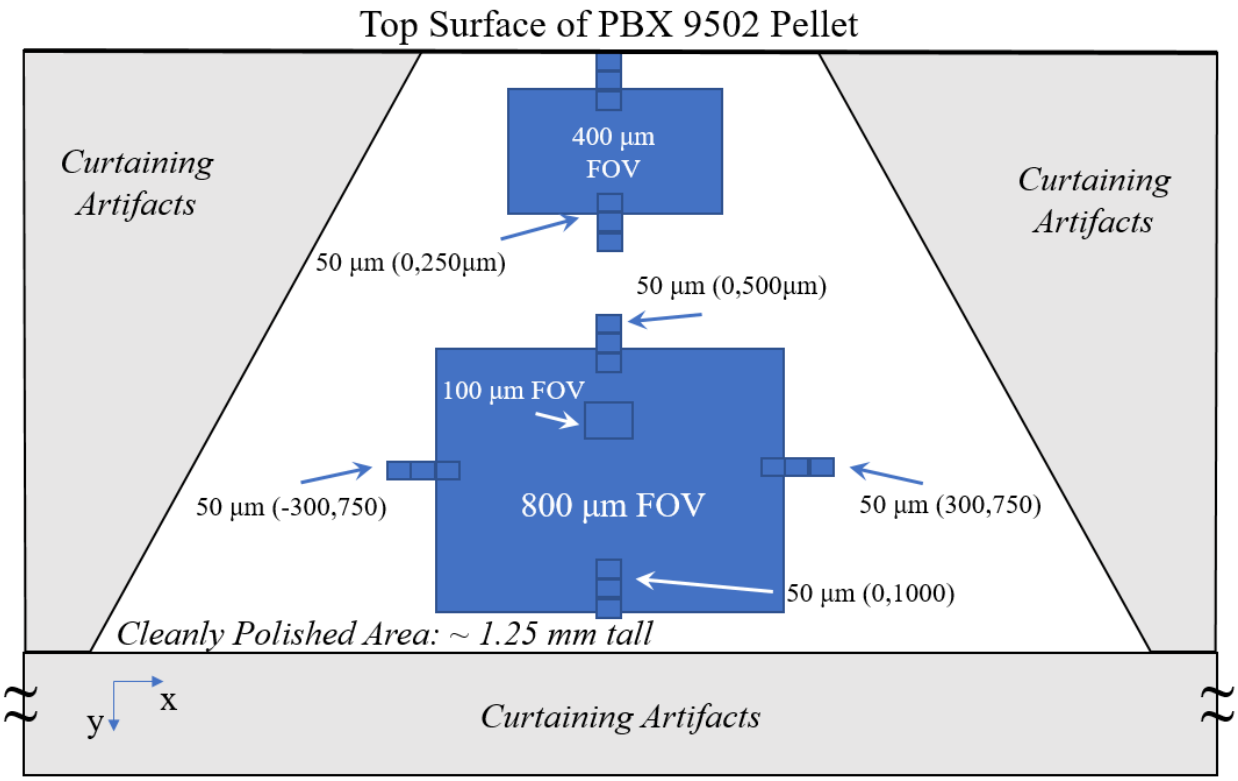

Figure 1. Approximate locations of all image locations for each cross-sectioned pellet.

2.3 Image Analysis

All image analysis for this work used the open source program ImageJ [36]. The two principal microstructural features measured were voids (including cracks) and grain size. Both were measured using standard techniques. Voids and cracks were identified and measured using a thresholding process in a similar way to many reports [37-39]. Briefly, ImageJ allows the user to define some pixel grayscale value to be the boundary value between two "materials" (e.g., solid vs. void), and then the grayscale image is segmented to binary by assigning all pixels with higher values to be one material and all pixels below to be the other. One part of the binary image or the other can then be selected and segmented for measurement. An example of void segmentation is given in Figure 2.

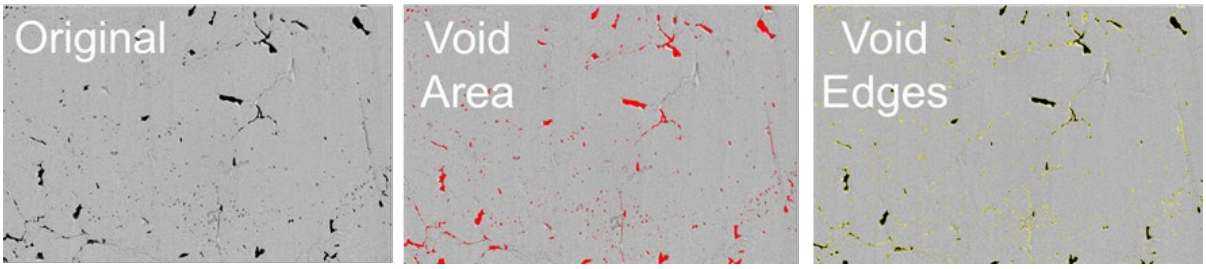

Figure 2. Original image shown along with segmented images with void area and with void edges highlighted. These are representative 50 µm FOV images.

As with any thresholding process, some amount of judgement is needed in determining exactly where the edges are, which "defects" count as voids, etc. For these measurements, any defect that was not obviously a surface scratch or artifact from the surface preparation was considered to be "void." The error of the technique was quantified by performing the thresholding process and measuring voids three separate times per image, where each repetition slightly changed the threshold value to be more generous or more restrictive for the void phase. This process results in void measurements that include both isolated voids and voids associated with microcrack openings. The grayscale values for cracks are more or less identical to isolated voids and so it is impossible to separate them automatically with the standard approach. To attempt to differentiate between these, a modified approach was used for a limited subset of the 50 μm FOV images for each sample to generally characterize the cracking. ImageJ has routines for measuring "particles" as well as total void content. If the particle parameters are chosen as broadly as possible, the total area of all particles will give the same result as the void content. However, additional restraints on particle aspect ratio ("circularity") and total size can be imposed. Circularity is defined as $4\pi(\text{Area}/\text{Perimeter}^2)$ and ranges from 0 to 1, where 0 is effectively a line and 1 is a perfect circle. For the crack measurements presented here, an *ad hoc* circularity range was set to between 0 and 0.2, based upon our interpretation of the images and judgment. It should be noted that some recent attempts have been made in the literature to segment defects into cracks vs. voids using other advanced segmentation techniques (relying on void aspect ratio and connectivity, for example) [33, 39, 40]. The images collected here could be reanalyzed with these new techniques in the future if needed.

Grain size measurements were also attempted for each sample. These were done manually using stereological techniques such as the line-intercept method because the grains were not generally well-defined [41]. The ion polishing did not sufficiently reveal grain boundaries for statistically significant analysis. Previous microstructural studies have indicated a wide range of potential particle sizes, suggesting that TATB particles tend to agglomerate [16, 42, 43]. Here, agglomeration was apparently observed at the larger FOV as "particles" outlined by cracks, while finer grain structure could be observed at the smaller FOV. The larger particles were often incompletely described by a visible interface and so actual agglomerate size measurements require some interpretation (and possibly extrapolation). However, since these measurements are being made on the pressed PBX microstructure, they provide additional information on the actual microstructure as opposed to traditional particle size measurements (e.g., laser light scattering or sieving [42-44]) that characterize the powder before formulating and pressing.

3. Results and Discussion

3.1 Thermal Cycling

Figure 3a shows the change in axial strain ($\Delta\varepsilon$) contributed from each hot or cold cycle versus the accumulated strain ($\Sigma\Delta\varepsilon$) of each hot or cold cycle for the virgin and recycled lots. Also included is the single data point for the hot and cold cycle of the single cycle CTE runs just to compare the first cycle growth. For both cold and hot cycles, the virgin lot initially grows slightly more than the recycled lot and also continues to grow more after 10 cycles. Figure 3b shows the strain value after

one full cycle (hot and cold) vs. the cycle number and summarizes the data in Figure 3a. Recall that one full cycle goes up to 153°C and down to -53°C with 30 minute holds at each endpoint temperature as well as at every pass through ambient (23°C). Overall, the virgin material exhibits more ratchet growth than the recycled material.

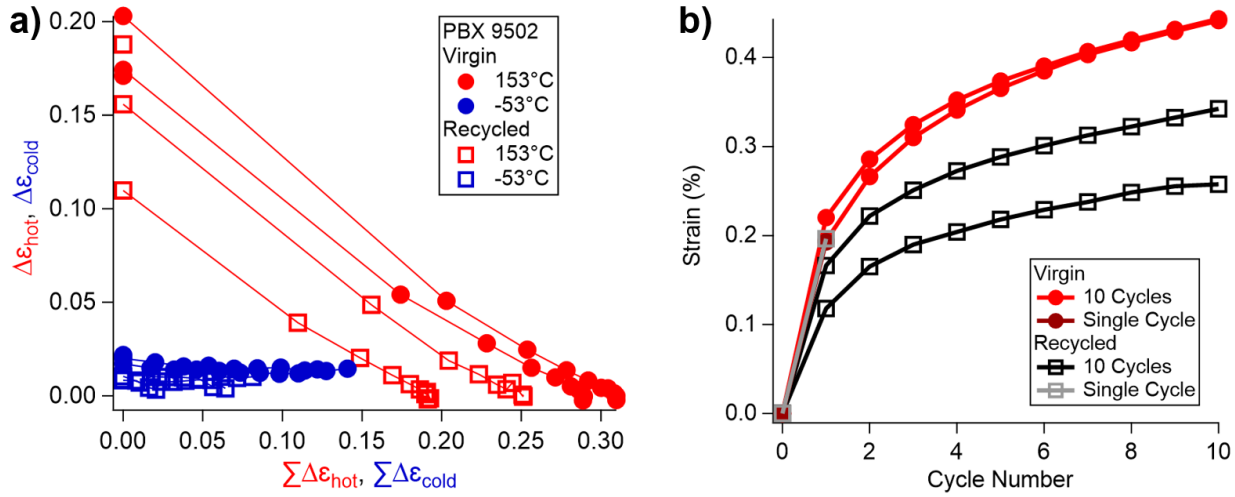

Figure 3. Hot and cold strain per cycle plotted against total strain accumulation for multiple pellets of each material (a). The total strain accumulation as a function of cycle number is shown in (b). In both cases, strain is derived from the displacement value recorded during the 30 minute hold at ambient after a full cycle.

Figure 4 shows strain vs. temperature by plotting the first cycle ramp from 153°C to -53°C for each sample. The CTE is the slope of the strain-temperature curve of the first cycle ramp. For consistency, the samples are broken out into two groups, those cycled only once and those eventually cycled 10 times, though there should be no real difference in the first cycle strain for a given lot. The cold behavior of both lots is similar, but the virgin lot exhibits a greater CTE, or more change in strain per °C, than the recycled lot. This may be related to the observed higher amount of accumulated strain from ratchet growth at warm temperatures shown in Figure 3.

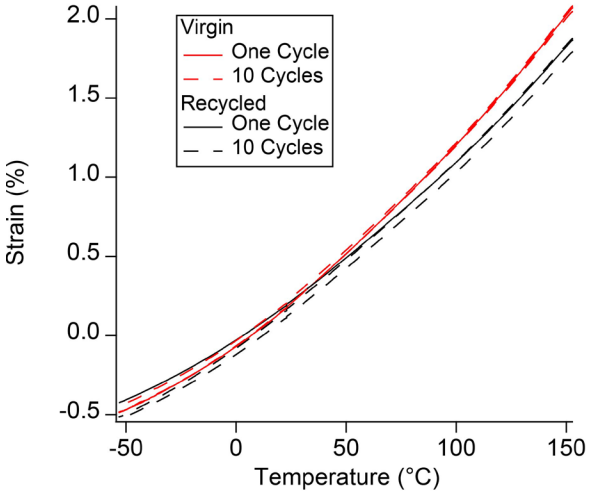

Figure 4. Strain vs. temperature of ramp from 153°C to -53°C for the first cycle only for each sample.

3.2 Void Size Analysis

Void size was measured for each sample using multiple fields of view. Figure 5 shows the typical variability in measured void content image to image for a given field of view, with the 50 µm FOV shown here because it has the highest number of images taken and the highest spatial resolution. Values from the images are plotted sequentially (the final plotted point is the overall average value for the sample), but the spatial data was retained and a statistical analysis of void content as a function of sample location could be performed if desired in the future. We did not observe any obvious trends in porosity as a function of sample location (e.g., moving from the edge to the center of the sample).

While most of the samples exhibited significant scatter in the measurements image to image, on average the porosity is consistent with expectations based on the bulk measurements. The large number of images is therefore considered a reasonably representative sampling of the pellets. The highest porosity calculated in any individual image is less than 5%, and generally ranges between 1.5% and 3.5%. Recall that the pellets were pressed to ~97% TMD and then ratchet grown another 0.2-0.4%, so this overall amount of porosity is approximately what would be expected. This gives confidence in the approach chosen to characterize the porosity.

Figure 5d shows the total void percentage for all six samples at 3 different FOV. The number of cycles (0, 1, or 10) and the lot are also indicated. Each sample shows the same trend of the smaller FOV yielding higher measured void content. This may be because the spatial resolution is worse at lower magnifications (greater FOV), so a higher number of potential voids are not likely resolved and so are missed by the threshold process. Also important to note is that if the accumulated sample area from all of the 50 µm FOV images is enough to be considered a representative sample for the entire pellet, then the 50 µm data alone would be the most believable due to having the highest spatial resolution.

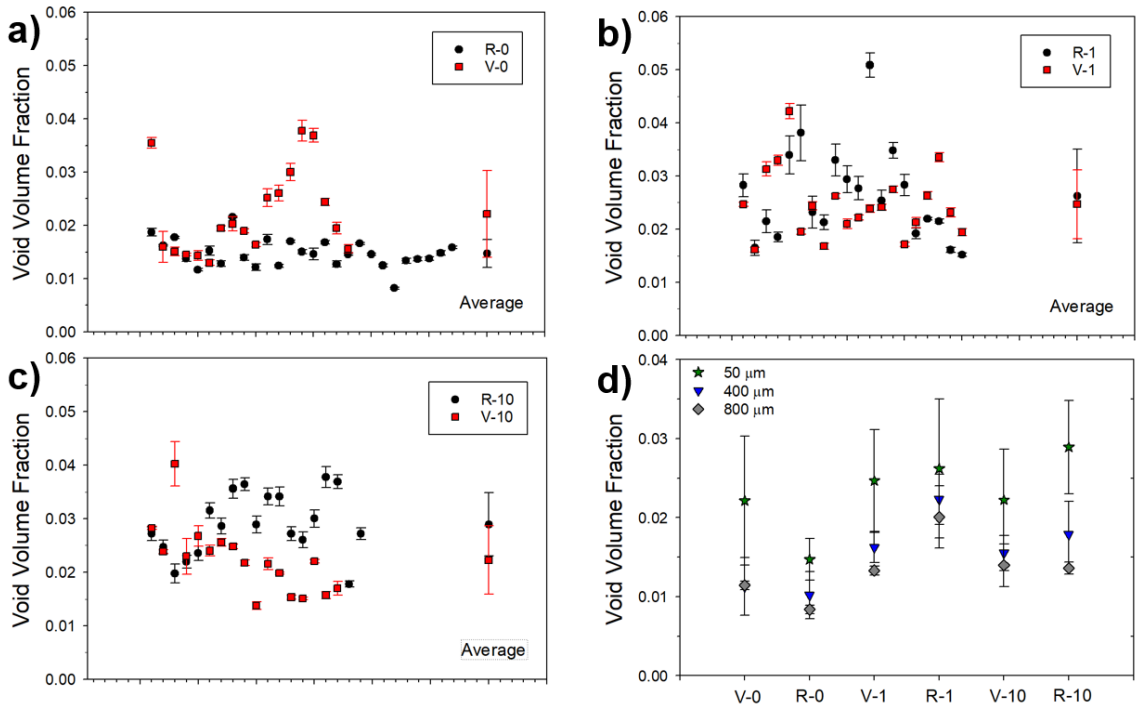

Figure 5. Image by image void content measurements for the pristine samples (a), samples after one cycle (b), and samples after 10 cycles (c) at the 50 µm FOV, showing typical variability. A summary of the void data all 3 FOV are shown for each sample in (d).

When comparing porosity measurements from void size analysis with the thermal cycling experiments, the microstructural measurements show some consistencies but also some limitations. For both lots of material, there is a clear difference in measured void content between pristine samples and those that have been ratchet grown. The difference is a little more obvious for the recycled samples than it is for the virgin samples. This is interesting because the ratchet growth was actually slightly higher in the virgin samples (see Figure 3). The total porosity is also slightly higher for both of the ratchet grown recycled samples, which is again inconsistent with the thermal cycling, but as Figure 5 shows, the error bars are quite large. Similarly, the total porosity in the once-cycled samples is not measurably different than the samples cycled ten times, since the standard deviations overlap significantly. So the general trend of ratchet growth increasing porosity is consistent between the thermal cycling data and the porosity measurements, but directly linking the amount of porosity to the measured amount of strain (and therefore volume growth) in the samples does not appear possible due to significant local variations in porosity.

A final note on total porosity. While the bulk porosity in the pellets should be ~3% based on bulk measurements, most of the measurements here show a lower total void content. This is most likely due to resolution issues and uncertainty in choosing threshold values for surface features which were not obviously voids. Figure 6 shows a 50 µm FOV sample with several features which, by eye, represent voids or other damage, but would not get picked up by the threshold process. It is possible to manually calculate the porosity from these images using stereological

techniques, but this would be prohibitively time consuming to gather appropriate statistics. Overall, the high-level takeaway from these measurements is that general trends are apparent, but quantifiable relationships between the porosity measured from the image segmentation and from the bulk uniaxial strain measurements are not achievable with the current methods. It is possible that more advanced stereological techniques could yield more useful results, and these may be pursued in future research. We also note that this is not the case for the subsequently discussed microcrack characterization, where clearly discernable differences in microcracking are apparent between the virgin and recycled lots.

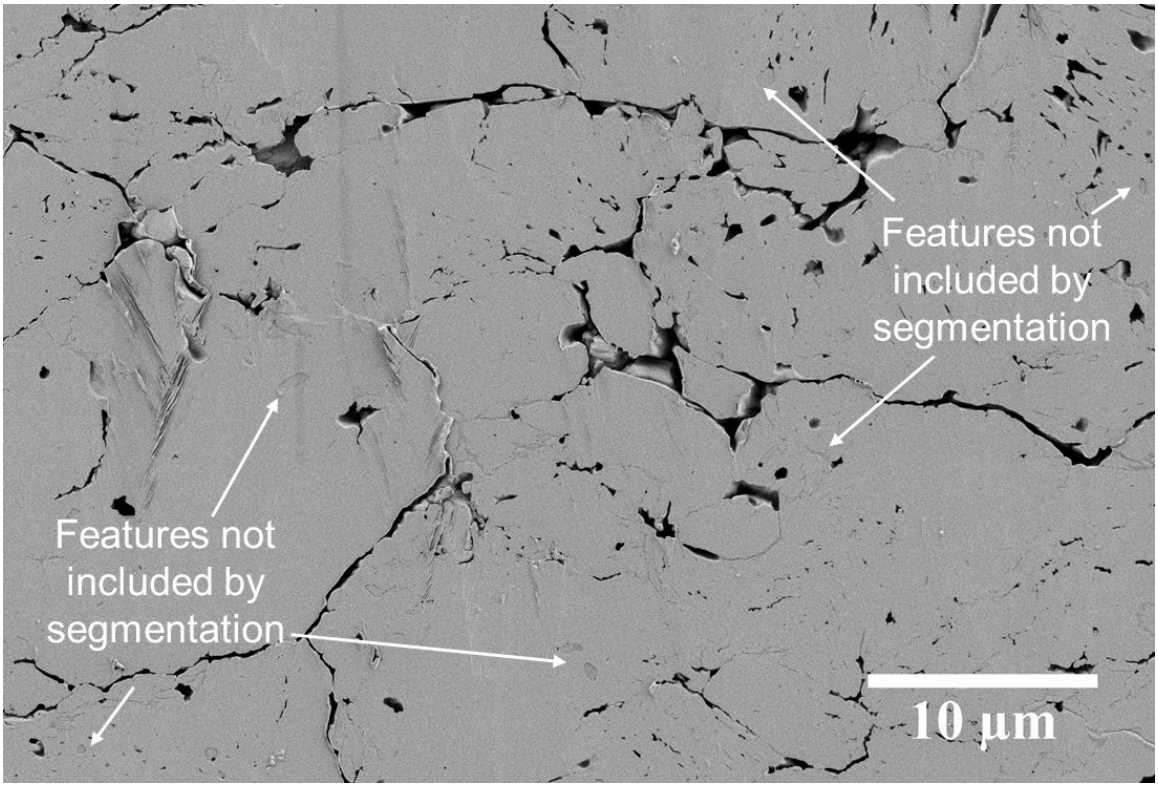

Figure 6. Typical image at 50 µm FOV, showing subtle features not segmentable (and therefore not measureable) by the threshold technique.

3.3 Grain Size Analysis

The concept of grain size or particle size for PBX 9502 is somewhat complicated compared to most traditional materials. TATB is quite difficult to grow as large crystals [45]. The fine particles can often clump when measured [46] and certainly tend to agglomerate once the formulation process with the binder has been finished [16]. Because of the graphitic structure of TATB crystal lattice, the crystals are thought to tend to form elongated grains [10, 24], though this seems to depend on processing, and most measurements of particle size have either been with sieves or using light scattering methods where sphericity must be assumed. Generally, TATB crystal grains are much smaller than 100 µm and often are smaller than 50 µm. However, the agglomerates can be larger, and recent modeling has shown that this length scale is also

important [25]. Here, a grain of TATB is defined by having a single crystallographic orientation, while an agglomerate is composed of grains with multiple orientations. A final length scale of importance observed in the literature is that of the PBX 9502 molding prills. These prills are the final product state before consolidating into pellets or other charges. The prills are low density spheroidal particles on the mm scale, consisting of aggregated crystals and binder, with a binder rich region on the outside [20, 47]. Despite charges being pressed at elevated temperatures so that the binder can flow and evenly coat the crystals, evidence of residual prill microstructure in pressed pieces has been observed [15, 20, 48]; however, we do not attempt to distinguish here between an agglomerate and a prill, primarily because the purpose of this work is to better identify the mechanisms of ratchet growth and associated microstructural changes (and secondly because of the inherent uncertainty in identifying *in situ* what was a prill before pressing).

For this study, using SEM images only, no evidence of residual prill structure was markedly observed. Note that the previous studies that had seen prill structure used either polarized light optical microscopy or x-ray tomography, which generate visual contrast in a much different way than SEM. PBX binder is furthermore notoriously difficult to spot with SEM, which is perhaps one reason determination of TATB particle sizes *in situ* has been elusive. However, the highest resolution images notably do show at least some evidence of distinct particles and their sizes. Representative images from several samples at the smallest FOV are shown in Figure 7, while an image from the 400 μm FOV is shown in Figure 8.

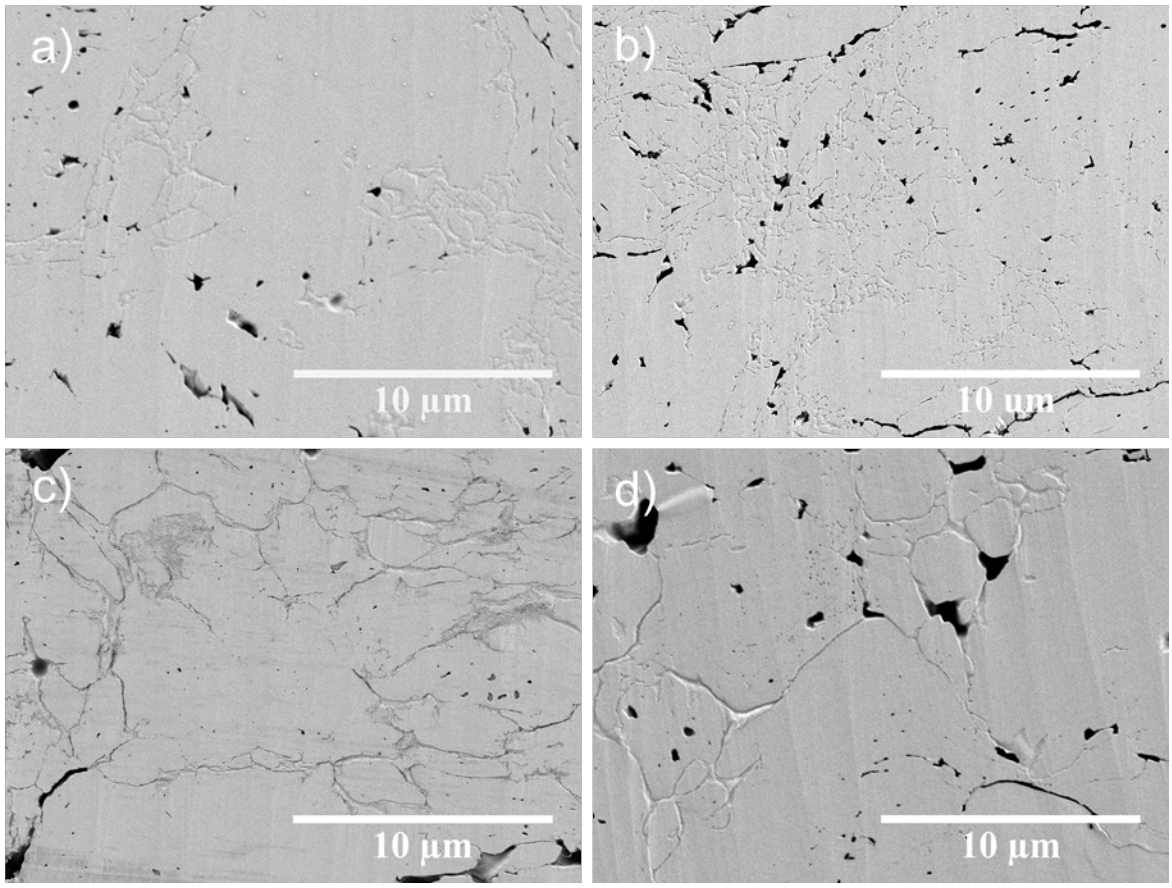

Figure 7. Highest resolution images taken of R-0 (a), R-10 (b), V-10 (c) and V-1 (d). Grain boundaries are often faint. Only the boundaries of the finest grains appear completely.

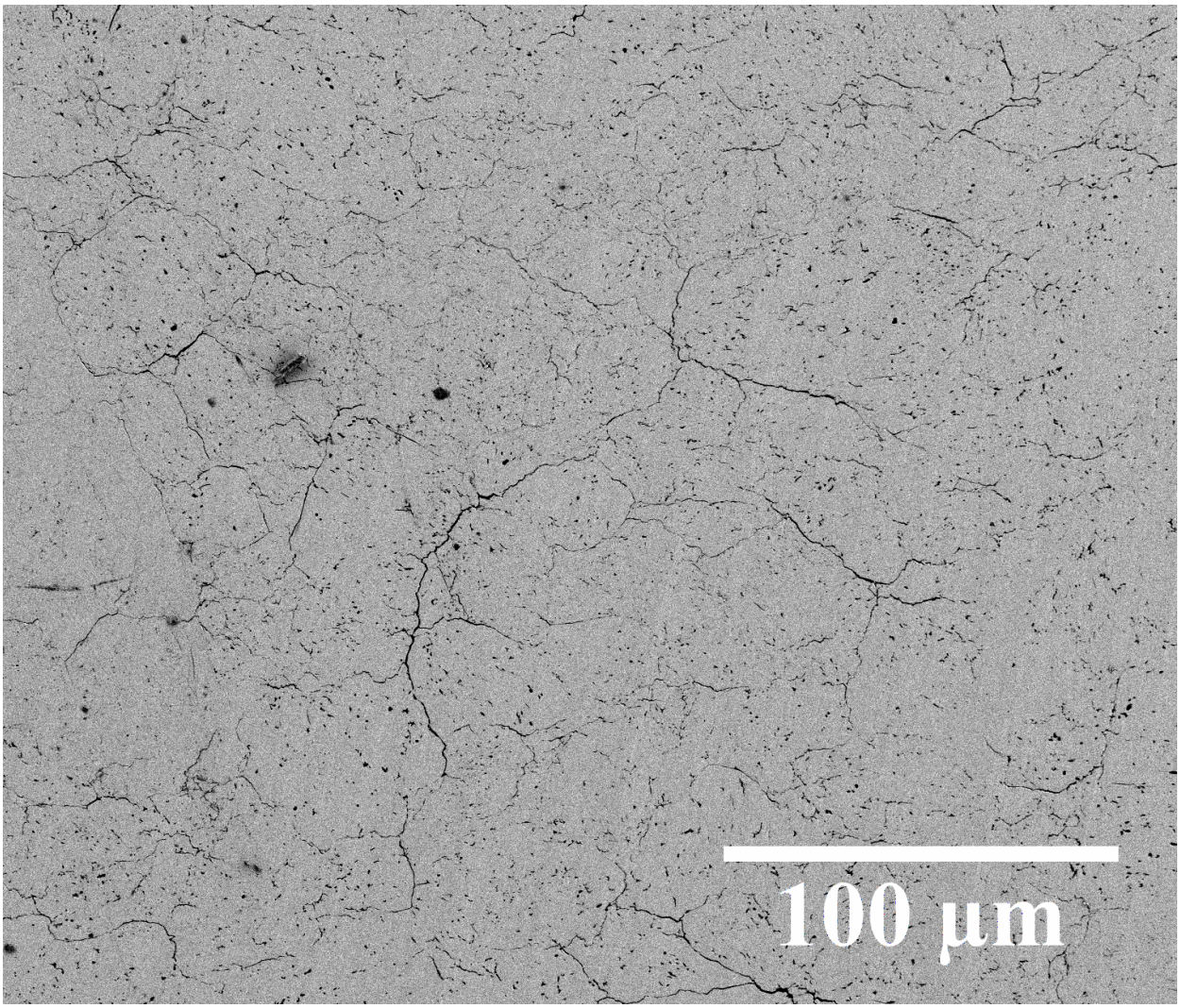

Figure 8. Typical microstructural image taken at the larger FOV. Apparent grain sizes, or more likely agglomerate sizes, are on the order of 20-50 microns.

Detailed stereological measurements of grain sizes are not possible, or at least not meaningful, due to the incomplete observation of grain boundaries in the figures. However, qualitatively, *the images appear to show two length scales of interest with respect to microfracture at particle interfaces*. The very fine grains, <10 μm diameter, can be visualized by their complete perimeter, including microfractured and intact portions. Larger grains (or agglomerates of grains) can only be interpreted by cracks that seem to propagate along their boundaries. Previous studies on this class of materials have shown strong evidence for intergranular fracture over transgranular due to relatively poor adhesion between the crystals and the binder [49-51]. This suggests that the cracking defines preexisting grain and/or agglomerate boundaries, i.e., the particles identified in the ratchet grown specimens are representative of the particles prior to thermal cycling.

3.4 Cracking

Since crack propagation appeared to highlight grain or agglomerate boundaries, a larger FOV was used to broadly quantify the number density of cracks as a function of material lot and ratchet growth. Figure 9 shows images from each sample at 400 μm FOV. For both lots of PBX 9502, cracking clearly increases as ratchet growth increases. This increase in cracking, shown at higher resolution and magnification in Figure 10, is especially interesting because the overall segmented porosity did not increase significantly. This strongly indicates that crack propagation is an important mechanism for ratchet growth, as suggested by some previous research [3, 5, 6, 27]. We note that porosity associated with relatively very small crack openings is difficult to segment from the images because of the pixel resolution size in comparison to the crack width; however, for long and abundant cracks, this void space may add up to a significant amount of additional porosity that is presently not being accounted for. Some other PBX 9502 studies simply note that "voids" of a variety of sizes are generated and do not differentiate between isolated voids and cracks [26, 52]. It is certainly possible that each of these studies are showing the same ratchet growth mechanism but the particularities of the techniques have caused them to be interpreted in slightly different ways.

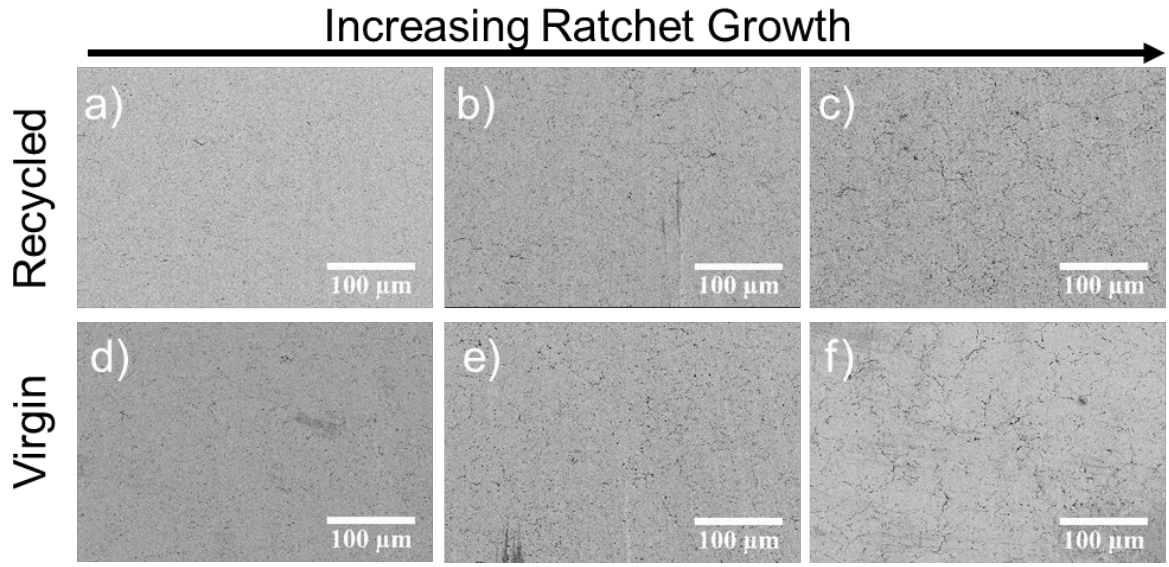

Figure 9. 400 μm FOV images of R-0 (a), R-1 (b), R-10 (c), V-0 (d), V-1 (e), and V-10 (f). Labels for the samples are also shown. The number density of cracks clearly increases with ratchet growth.

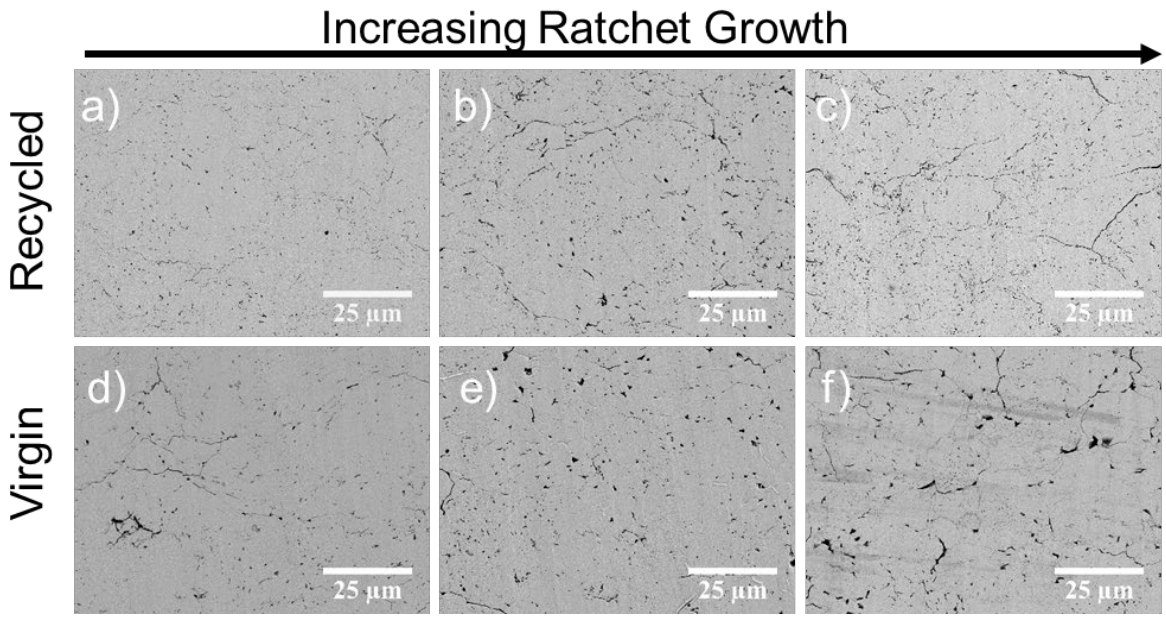

Figure 10. 100 µm FOV images of R-0 (a), R-1 (b), R-10 (c), V-0 (d), V-1 (e), and V-10 (f). Increased cracking as a function of ratchet growth can clearly be seen.

All of the images in Figure 9 were taken from identical sample coordinates for sampling consistency, and the same is true for Figure 10. While the increase in cracking from pristine to once-cycled virgin material (Fig 10d vs. Fig 10e) is not clear at this particular sample location, the 50 µm FOV images compiled together clearly demonstrate increased cracking. For brevity, the 20+ images for each sample are not shown here, but Table 2 summarizes the crack findings. There are several ways to characterize extent of cracking manually, such as crack length, crack density, crack opening, etc. Here, three crack parameters were calculated for each sample using 5 images at 50 µm FOV from identical locations in each sample (X=0 and Y=100, 300, 500, 1000, 1200). Each parameter can either be determined directly from the segmentation or calculated simply using measured values. The total number of cracks is given by the particle tracking routine in ImageJ. The Feret diameter is the maximum distance between any 2 points on the perimeter of a particle, or in this case a void or crack, which is effectively a crack length measurement. Finally, the total area of all cracks is measured and compared to the image size, giving the % cracked area.

Table 2. Crack characteristics as determined from image segmentation and analysis

Sample	# Cracks	Feret Diameter (µm)	% Cracked Area
R-0	108 ± 13	0.92 ± 0.25	0.56 ± 0.27
R-1	123 ± 27	1.04 ± 0.17	1.27 ± 0.34
R-10	65 ± 20	1.98 ± 0.63	1.51 ± 0.65
V-0	70 ± 22	1.93 ± 0.75	1.39 ± 0.97
V-1	103 ± 29	1.44 ± 0.18	1.70 ± 0.90
V-10	92 ± 7	1.69 ± 0.39	2.45 ± 0.82

Table 2 seems to demonstrate a few interesting trends. First, as inferred from the larger scale FOV images, the cracking exhibits primarily as dispersed individual microcracks (of small Feret diameter). The average crack size is perhaps a little misleading because the segmentation routine often broke up what seemed (be eye) to be large cracks into multiple smaller cracks. Still, the longest individual non-branching crack observed in the images was around 20 μm, and in most images, most of the cracks were smaller than 10 μm. Second, in the recycled samples, the Feret diameter increases with the number of cycles, while for the virgin material this trend is not observed, and indeed the standard deviation of the measurements overlap for the virgin material (but not the recycled). Third, in both sets of materials the total number of cracks increases as the material goes from pristine to once-cycled, then falls for the samples cycled ten times. This appears to be evidence of crack coalescence, in light of the final result that, importantly, the cracked area percentage exhibits clear trends of increasing as the ratchet growth increases. This effect is more dramatic for the virgin material than for the recycled material. This is consistent with the strain measurements from Figure 3, where the virgin material grew more than the recycled material. Recall from Figure 5 that the total void content significantly increased from pristine to once-cycled but then stagnated (within error). The fact that the cracking continues to increase while total void content does not is likely due to the limits of the segmentation analysis, with cracks propagating between voids (and/or voids serving as crack nucleation sites) and effectively absorbing voids as they grow. These results show that intergranular void growth and coalescence into cracks is an important mechanism for ratchet growth and suggest that they should be accounted for in future mesoscale models.

3.5 Implications for Accurate Mesoscale Modeling

The results of this study show that intergranular microcracking is an important mechanism of ratchet growth, i.e., voids associated with microcrack openings account for a substantial portion of observed increases in bulk porosity during thermal cycling. This suggests that mesoscale models of ratchet growth in PBX 9502 need to resolve grain-interfaces and intergranular cracking. Moreover, the high-fidelity measurements of particle, void, and crack characteristics presented in this work provide an important calibration and validation dataset for mesoscale models, in particular for direct numerical simulation (DNS) of microstructure [49, 53] and micromechanical (analytical) homogenization models [24, 25, 54, 55]. We are currently working to incorporate the current results into both of these types of models.

Conclusions

A comprehensive study of PBX 9502 specimens was conducted using virgin and recycled lots of material, characterizing the microstructure as a function of thermal cycling-induced ratchet growth. Ion polishing was successfully used to prepare surfaces for SEM study of sufficient quality for quantitative measurements. The combination of extensive microstructural characterization and thermal cycling data reveal some important facts about thermomechanical behavior of PBX 9502. The virgin lot of PBX 9502 exhibited a higher amount of ratchet growth than did the recycled lot. This growth, measured with TMA, was found by SEM analysis to be primarily enabled by microcrack nucleation and growth, which was observed to be significantly greater in the virgin material. Particle sizes measured by SEM were in reasonable agreement

with literature results using pre-pressed powders, but also showed a larger length scale of particle agglomeration that is also consistent with other recent studies. These findings have significant implications for mesoscale modeling approaches, both in terms of informing the underlying micromechanical mechanisms of ratchet growth and in providing a quantitative dataset for model calibration and validation. Further, segmented images from this study could be used for constructing and evaluating direct numerical simulations of real PBX materials.

Acknowledgements

The authors would like to thank Darla Thompson and Racci DeLuca for assistance with the thermal cycling measurements. Barry Ritchey and Adam Pimentel collected the SEM images. Daniel Trujillo provided direction and facilitated LANL-Sandia collaboration. Funding for this work was provided by the System Engineering Group at Los Alamos National Laboratory. Los Alamos National Laboratory is operated by Triad National Security, LLC, for the National Nuclear Security Administration of U.S. Department of Energy (Contract No. 89233218CNA000001). This paper describes objective technical results and analysis. Any subjective views or opinions that might be expressed in the paper do not necessarily represent the views of the U.S. Department of Energy or the United States Government. Sandia National Laboratories is a multimission laboratory managed and operated by National Technology & Engineering Solutions of Sandia, LLC, a wholly owned subsidiary of Honeywell International Inc., for the U.S. Department of Energy's National Nuclear Security Administration under contract DE-NA0003525.

References

[1] J.L. Maienschein, F. Garcia, Thermal expansion of TATB-based explosives from 300 to 566 K, Thermochim. Acta, 384 (2002) 71-83.

[2] D.G. Thompson, G.W. Brown, B. Olinger, J.T. Mang, B. Patterson, R. DeLuca, S. Hagelberg, The Effects of TATB Ratchet Growth on PBX 9502, Propellants Explos. Pyrotech., 35 (2010) 507-513.

[3] C.S. Woznick, D.G. Thompson, R. DeLuca, B.M. Patterson, T.A. Shear, Thermal cycling and ratchet growth of as-pressed TATB pellets, 1979 (2018) 060011.

[4] H.F. Rizzo, J.R. Humphrey, J.R. Kolb, Growth of 1,3,5-Triamino-2,4,6,-Trinitrobenzene (TATB). II. Control of growth by use of high Tg polymeric binders, 6 (1981) 27-36.

[5] R.N. Mulford, J.A. Romero, Sensitivity of the TATB-based explosive PBX-9502 after thermal expansion, 429 (1998) 723-726.

[6] R.B. Schwarz, Model for ratchet growth in PBX 9502, Acta Mater., 180 (2019) 170-179.

[7] L.G. Hill, D.G. Thompson, H.H. Cady, On the ratchet growth of TATB-based explosives, Los Alamos National Lab.(LANL), Los Alamos, NM (United States), 2011.

[8] R.H. Gee, A. Maiti, L.E. Fried, Mesoscale modeling of irreversible volume growth in powders of anisotropic crystals, 90 (2007) 254105.

[9] H.H. Cady, A.C. Larson, The crystal structure of 1,3,5-triamino-2,4,6-trinitrobenzene, Acta Crystallographica, 18 (1965) 485-496.

[10] J.D. Yeager, D.J. Luscher, S.C. Vogel, B. Clausen, D.W. Brown, Neutron Diffraction Measurements and Micromechanical Modelling of Temperature-Dependent Variations in TATB Lattice Parameters, Propellants Explos. Pyrotech., 41 (2016) 514-525.

[11] R.B. Schwarz, G.W. Brown, D.G. Thompson, B.W. Olinger, J. Furmanski, H.H. Cady, The Effect of Shear Strain on Texture in Pressed Plastic Bonded Explosives, Propellants Explos. Pyrotech., 38 (2013) 685-694.

[12] C.B. Skidmore, T.A. Butler, C.W. Sandoval, The Elusive Coefficients of Thermal Expansion in PBX 9502, 2003.

[13] D. Bedrov, O. Borodin, G.D. Smith, T.D. Sewell, D.M. Dattelbaum, L.L. Stevens, A molecular dynamics simulation study of crystalline 1,3,5-triamino-2,4,6-trinitrobenzene as a function of pressure and temperature, J. Chem. Phys., 131 (2009) 224703.

[14] L. Valenzano, W.J. Slough, W. Perger, Accurate prediction of second-order elastic constants from first principles: PETN and TATB, 1426 (2012) 1191-1194.

[15] J.D. Yeager, L.A. Kuettner, A.L. Duque, L.G. Hill, B.M. Patterson, Microcomputed X-Ray Tomographic Imaging and Image Processing for Microstructural Characterization of Explosives, Materials, 13 (2020) 4517.

[16] P.D. Peterson, D.J. Idar, Microstructural Differences between Virgin and Recycled Lots of PBX 9502, Propellants Explos. Pyrotech., 30 (2005) 88-94.

[17] D.M. Hoffman, A.T. Fontes, Density Distributions in TATB Prepared by Various Methods, 35 (2010) 15-23.

[18] M.B. Talawar, A.P. Agarwal, M. Anniyappan, G.M. Gore, S.N. Asthana, S. Venugopalan, Method for preparation of fine TATB (2–5μm) and its evaluation in plastic bonded explosive (PBX) formulations, J. Hazard. Mater., 137 (2006) 1848-1852.

[19] A.W. Campbell, Diameter Effect and Failure Diameter of a TATB-Based Explosive, 9 (1984) 183-187.

[20] T.M. Willey, L. Lauderbach, F. Gagliardi, B. Cunningham, K.T. Lorenz, J.I. Lee, T. van Buuren, R. Call, L. Landt, G. Overturf, Comprehensive Characterization of Voids and Microstructure in TATB-based Explosives from 10 nm to 1 cm: Effects of Temperature Cycling and Compressive Creep, Fourteenth International Detonation Symposium, Coeur d'Alene, ID, United States, 2010.

[21] W.L. Perry, A.L.H. Duque, J.D. Yeager, L.G. Hill, V.H. Whitley, Can we predict how nano-scopic voids affect explosive performance?, 2272 (2020) 070036.

[22] N.K. Rai, O. Sen, H.S. Udaykumar, Macro-scale sensitivity through meso-scale hotspot dynamics in porous energetic materials: Comparing the shock response of 1,3,5-triamino-2,4,6-trinitrobenzene (TATB) and 1,3,5,7-tetranitro-1,3,5,7-tetrazoctane (HMX), 128 (2020) 085903.

[23] N.K. Rai, M.J. Schmidt, H.S. Udaykumar, Collapse of elongated voids in porous energetic materials: Effects of void orientation and aspect ratio on initiation, Physical Review Fluids, 2 (2017) 043201.

[24] K.C. Bennett, D.J. Luscher, M.A. Buechler, J.D. Yeager, A micromechanical framework and modified self-consistent homogenization scheme for the thermoelasticity of porous bonded-particle assemblies, International Journal of Solids and Structures, DOI https://doi.org/10.1016/j.ijsolstr.2018.02.001(2018).

[25] K.C. Bennett, M. Zecevic, D.J. Luscher, R.A. Lebensohn, A thermo-elastoplastic self-consistent homogenization method for inter-granular plasticity with application to thermal ratcheting of TATB, Advanced Modeling and Simulation in Engineering Sciences, 7 (2020) 3.

[26] T.M. Willey, D.M. Hoffman, T. van Buuren, L. Lauderbach, R.H. Gee, A. Maiti, G.E. Overturf, L.E. Fried, J. Ilavsky, The Microstructure of TATB-Based Explosive Formulations During Temperature Cycling Using Ultra-Small-Angle X-Ray Scattering, Propellants Explos. Pyrotech., 34 (2009) 406-414.

[27] J.T. Mang, R.P. Hjelm, Fractal Networks of Inter-Granular Voids in Pressed TATB, Propellants Explos. Pyrotech., 38 (2013) 831-840.

[28] A.L. Nichols, C.M. Tarver, A Statistical Hot Spot Reactive Flow Model for Shock Initiation and Detonation of Solid High Explosives, Twelfth International Detonation Symposium, International Detonation Symposium, San Diego, CA, 2002.

[29] S. Kim, A. Barua, Y. Horie, M. Zhou, Ignition probability of polymer-bonded explosives accounting for multiple sources of material stochasticity, 115 (2014) 174902.

[30] J.R. Kolb, H.F. Rizzo, Growth of 1,3,5-Triamino-2,4,6-trinitrobenzene (TATB) I. Anisotropic thermal expansion, Propellants Explos. Pyrotech., 4 (1979) 10-16.

[31] D.G. Thompson, C.S. Woznick, R. DeLuca, The volumetric coefficient of thermal expansion of PBX 9502, Los Alamos National Lab.(LANL), Los Alamos, NM (United States), 2018.

[32] R.R. Wixom, A.S. Tappan, A.L. Brundage, R. Knepper, M.B. Ritchey, J.R. Michael, M.J. Rye, Characterization of pore morphology in molecular crystal explosives by focused ion-beam nanotomography, J. Mater. Res., 25 (2010) 1362-1370.

[33] C.D. Molek, E.J. Welle, J.O. Mares Jr, J. Vitarelli, D. Barrett Hardin, M. Stuthers, Impact of void structure on initiation sensitivity, Propellants Explos. Pyrotech., 45 (2020) 236-242.

[34] J.D. Olles, R.R. Wixom, R. Knepper, A.S. Tappan, Observations of shock-induced chemistry with subnanosecond resolution, Appl. Phys. Lett., 114 (2019) 214102.

[35] A.S. Tappan, R.R. Wixom, R. Knepper, Critical detonation thickness in vapor-deposited hexanitroazobenzene (HNAB) films with different preparation conditions, Fifteenth International Detonation Symposium, Office of Naval Research, San Francisco, CA, 2014.

[36] C.A. Schneider, W.S. Rasband, K.W. Eliceiri, NIH Image to ImageJ: 25 years of image analysis, Nature Methods, 9 (2012) 671-675.

[37] F. Papadopulos, M. Spinelli, S. Valente, L. Foroni, C. Orrico, F. Alviano, G. Pasquinelli, Common Tasks in Microscopic and Ultrastructural Image Analysis Using ImageJ, Ultrastructural Pathology, 31 (2007) 401-407.

[38] N. Vanderesse, É. Maire, A. Chabod, J.Y. Buffière, Microtomographic study and finite element analysis of the porosity harmfulness in a cast aluminium alloy, Int. J. Fatigue, 33 (2011) 1514-1525.

[39] Y. Li, Y. Zhang, E.-H. Yang, K.H. Tan, Effects of geometry and fraction of polypropylene fibers on permeability of ultra-high performance concrete after heat exposure, Cem. Concr. Res., 116 (2019) 168-178.

[40] J.J. Williams, Z. Flom, A.A. Amell, N. Chawla, X. Xiao, F. De Carlo, Damage evolution in SiC particle reinforced Al alloy matrix composites by X-ray synchrotron tomography, Acta Mater., 58 (2010) 6194-6205.

[41] E.E. Underwood, Quantitative stereology for microstructural analysis, Microstructural analysis, Springer1973, pp. 35-66.

[42] A.K. Nandi, S.M. Kasar, U. Thanigaivelan, M. Ghosh, A.K. Mandal, S.C. Bhattacharyya, Synthesis and Characterization of Ultrafine TATB, J. Energ. Mater., 25 (2007) 213-231.

[43] D. Luscher, J. Yeager, B. Clausen, S. Vogel, A. Higginbotham Duque, D. Brown, Using Neutron Diffraction to Investigate Texture Evolution During Consolidation of Deuterated Triaminotrinitrobenzene (d-TATB) Explosive Powder, Crystals, 7 (2017) 138.

[44] A. Duncan, Inter-and intra-laboratory sieve analysis of TATB, Mason and Hanger-Silas Mason Co., Inc., Amarillo, Tex.(USA), 1977.

[45] B.M. Dobratz, The Insensitive High Explosive Triaminotrinitrobenzene (TATB): Development and Characterization—1888 to 1994, Los Alamos National Laboratory, 1995.

[46] C. Honodel, J. Humphrey, R. Weingart, R. Lee, P. Kramer, Shock initiation of TATB formulations, Proceedings of the 7th Symposium (International) on Detonation, 1982, pp. 425-434.

[47] G.W. Brown, D.G. Thompson, R. DeLuca, E.L. Hartline, S.I. Hagelberg, DENSITY-DEPENDENT ACOUSTIC PROPERTIES OF PBX 9502, AIP Conference Proceedings, 1195 (2009) 373-376.

[48] J. Kinney, T. Willey, G. Overturf, On the nature of variations in density and composition within TATB-based plastic bonded explosives, Lawrence Livermore National Laboratory, Livermore, CA (United States), 2006.

[49] V.W. Manner, J.D. Yeager, B.M. Patterson, D.J. Walters, J.A. Stull, N.L. Cordes, D.J. Luscher, K.C. Henderson, A.M. Schmalzer, B.C. Tappan, In Situ Imaging during Compression of Plastic Bonded Explosives for Damage Modeling, Materials, 10 (2017) 638.

[50] S.J.P. Palmer, J.E. Field, J.M. Huntley, Deformation, Strengths and Strains to Failure of Polymer Bonded Explosives, Proc. R. Soc. London, Ser. A, 440 (1993) 399-419.

[51] P.J. Rae, H.T. Goldrein, S.J.P. Palmer, J.E. Field, A.L. Lewis, Quasi-Static Studies of the Deformation and Failure of β-HMX Based Polymer Bonded Explosives, Proceedings: Mathematical, Physical and Engineering Sciences, 458 (2002) 743-762.

[52] J. Dallman, J. Wackerle, Temperature-dependent shock initiation of TATB-based high explosives, 10th International Symposium on Detonation, Boston, MA, USA, 1993.

[53] D.J. Walters, D.J. Luscher, J.D. Yeager, 3D micromechanical simulation of PBX composites, AIP Conference Proceedings, AIP Publishing LLC, 2020, pp. 070052.

[54] K.C. Bennett, D.J. Luscher, Effective thermoelasticity of polymer-bonded particle composites with imperfect interfaces and thermally expansive interphases, Journal of Elasticity, 136 (2019) 55-85.

[55] E.C. Bryant, K.C. Bennett, N.A. Miller, A. Misra, Multiscale plasticity of geomaterials predicted via constrained optimization-based granular micromechanics, International Journal for Numerical and Analytical Methods in Geomechanics, 2021, https://doi.org/10.1002/nag.3320.